Chapter 3

Platinum nanowire

resonator

The most complete of my projects was the fabrication and measurement of doubly-clamped platinum nanowire resonators. It is complete in the sense that we conceived, fabricated, and measured this type of device and explained its behavior from theory. It is the first instance of a resonator fabricated from "bottom-up" materials. This device exhibited fascinating non-linear behavior which will become important to future research in nanomechanical resonators as dimension get even smaller.

3.1 Introduction

Fabrication and readout of mechanical resonators of increasingly small size is an active and interesting area of research, and critical for the development of high-frequency nanoelectromechanical systems (NEMS) for low mass, high sensitivity devices. Cutting-edge applications of NEMS require both high responsivity and ultrahigh-frequency devices for sensing applications such as sub-attonewton, high-frequency force sensing

and electrometry as well as fundamental physical studies of dissipation mechanisms and mechanical systems in the quantum mechanical regime.[1]

As NEMS shrink down to the single molecule regime, integration with top-down fabrication techniques will be a crucial challenge. Researchers typically employ these top-down techniques to create mechanical structures out of semiconductor materials such as silicon[2], silicon carbide[3], gallium arsenide[4] and aluminum nitride.[5] However, conventional techniques yield device dimensions that are limited by the resolution of electron-beam lithography, etch roughness, the synthesis of epitaxially grown substrates, and other factors. As a result, there has been much interest in fabricating devices from "bottom-up" materials such as carbon nanotubes[6] and semiconductor[7] and metal nanowires.[8] These bottom-up materials can be synthesized in diameters down to single-nanometers which is smaller than can be achieved with conventional e-beam lithography. These materials can be atomically perfect, reducing surface dissipation due to defects. These advantages and others have led researchers to investigate nanomaterials for a large variety of uses.

3.2   Nanoresonator fabrication

We have developed a process to locate nanomaterials randomly deposited on a substrate and to lithographically align to them, an example of which is shown in an SEM image in Figure 3.1, left. To do this, it is necessary to fabricate a grid and alignment marks on the chip before adding the nanowires. A PMMA bi-layer (2% 495 mol wt, 2% 950 mol wt) was spun at 5000 RPM onto the surface of the chip. The purpose of the bi-

layer is to create an undercut resist patter that will improve a later lift-off. The PMMA coated chip is baked on a hot plate at 180°C for 5 min. Electron-beam lithography is used to expose a grid pattern and alignment crosses on the chip. After developing the PMMA in 3:1 IPA (isopropyl alcohol):MIBK (methyl isobutylketone), 5 nm and 80 nm of Cr and Au, respectively, are evaporated onto the surface. The PMMA is removed with acetone in a lift-off process, leaving the metalized alignment marks and grid.
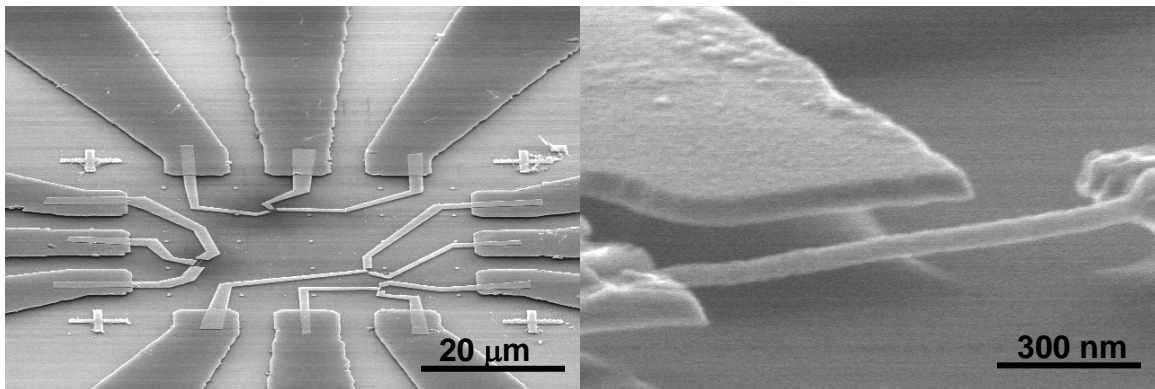

Figure 3.1: Left—low magnification image of pads, grid and alignment marks. Right—high magnification image of nanowire resonator.

To fabricate a suspended platinum nanowire, we first synthesize the nanowires by the electro-deposition method described in Section 2.1. Next, the wires are suspended in a solvent, chloroform, which dissolves the polycarbonate membrane. Drops of the suspension are deposited on a degenerately doped silicon chip with a 300 nm thick thermally grown silicon dioxide layer. As each drop dries, wires are left randomly distributed on the surface. To place electrical leads on the wires, we need to locate the positions of candidate wires. An atomic force microscope (AFM) is used to map the topology of the surface, revealing the position of nanowires with respect to the grid. The

mapping can also be carried out with an optical microscope because of the strong light scattering of the nanowires, but with much lower accuracy. A PMMA bi-layer is spun on, identical to the last, and contact leads are defined using electron beam lithography. Finally, Cr/Au is evaporated and lifted off, leaving a Pt nanowire which is electrically accessible. The nanowire is suspended by wet etching for 1 min in 8% buffered hydrofluoric acid, which etches about 100 nm. Critical point drying completes the process, avoiding the damaging effects of the surface tension of the evaporating solvent. The right image in Figure 3.1 shows the final device. The third electrode, not in contact with the wire, was meant to be a capacitive gate. It was not used in the initial experiment due to a broken electrical lead on the sample holder.

3.3   NEMS theory and measurement techniques

Mechanical resonance modes of cantilevers and doubly-clamped beams are well understood. Modeling as an unstrained doubly-clamped beam yields a predicted fundamental mechanical resonance frequency f_0 given by[9]

$$f_0 = \frac{22.4}{2\pi} \frac{R}{2L^2} \sqrt{\frac{Y}{\rho}}, \quad (1)$$

where Y is the Young's modulus, ρ is the density of the beam, R is the beam radius and L is the beam length. Using the bulk values for the Young's modulus and density of platinum (168 GPa and 21090 kg/m^3, respectively[10]) and the dimensions of a typical device (length of 1.3 μm and diameter of 43 nm), equation (1) predicts a fundamental

frequency of 64 MHz, so that experiments will be in the microwave regime. This turns

out to be lower than the measured response; reasons for this will be discussed later.
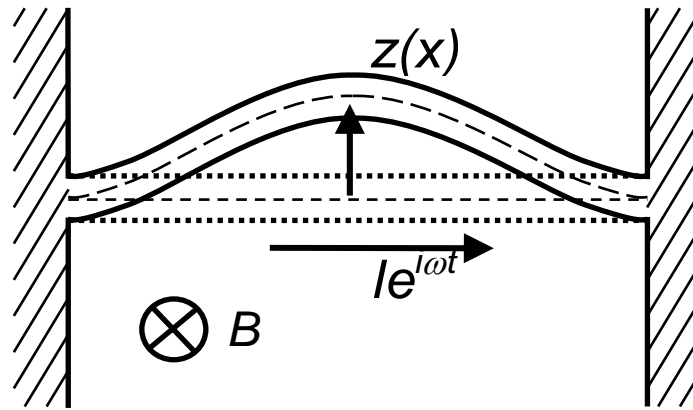

Figure 3.2: Schematic of magnetomotive actuation where B is the magnetic field, I is the current and z is the displacement of the beam.

In nanomechanical systems research, a common method of actuating and

detecting such a device is the magneto-motive method pioneered in the group of Prof.

Michael Roukes here at Caltech[2] and used by many others[11]. A diagram of this scheme is

shown in Figure 3.2. In this technique, the resonator is placed in a large magnetic field

oriented perpendicular to the beam. The resonator is integrated with a wire which is

connected to electrical leads, through which an AC current is passed. The wire

experiences a Lorentz force due to the time varying current in a magnetic field. At

resonance, the resonator (and integrated wire) is moving through a magnetic field,

producing a back electromotive field (EMF) that is detected as a change in the power

delivered to the device. The back EMF will maximize when the frequency of the current

through the resonator matches its resonant frequency. In standard top-down NEMS the

current carrying wire is integrated into the structure by evaporating gold leads onto the

resonator. In contrast, in this hybrid bottom-up/top-down device, the resonator is the wire.

The resonator can be modeled as an *LCR* tank circuit with an intrinsic resistance that accounts for the intrinsic dissipation of the vibrating beam.[12] The value of the capacitance, inductance and resistance in this model can be written as,

$$C_m = \frac{m}{\xi l^2 B^2}, L_m = \frac{\xi l^2 B^2}{m}, R_m = \frac{\xi l^2 B^2}{\omega_0^2 m} Q, \quad (2)$$

respectively, where l is the length of the beam, m is the (effective) mass of the beam, B is the magnetic field, ω_0 is the natural frequency and ξ is a numerical factor (0.83 for the fundamental mode) that depends on the mode shape. The quality factor that appears in R_m is the unloaded Q, accounting for intrinsic dissipation within the beam. The circuit model for the resonator is shown in Figure 3.3 where R_e is the intrinsic electrical resistance of the nanowire, i.e., the two probe resistance of the wire including contact and lead resistance. In our R_e devices, was around 500 Ω.
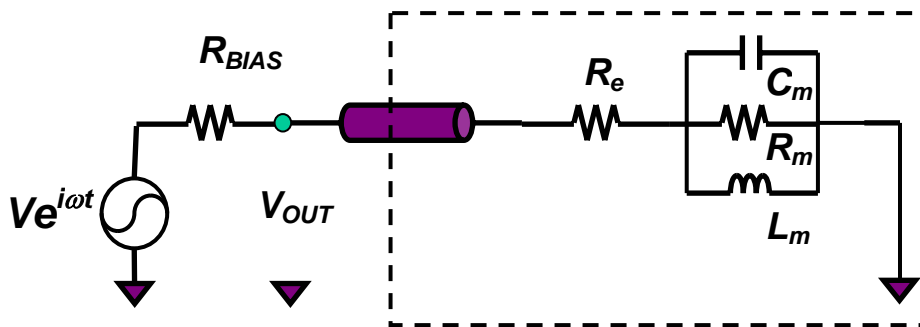

Figure 3.3: Electrical schematic showing measurement setup. All components within the dashed box are in a liquid He dewar at 4.2 K.

The method of detecting the reflected power is specifically designed for samples that are well matched to RF power generating equipment. Typical top-down NEMS devices have $R_e \sim 10\text{-}100$ Ω and $R_m \sim 1$ Ω while RF sources are generally designed to be impedance matched to 50 Ω. However, our devices have a resistance R_e at least one order of magnitude higher. A small change in the total resistance of the device, $R_e + R_m$, will result in very small change in the reflected power, requiring a modification of the method. In the traditional scheme, the drive and detected signal utilize the same port. Our modified circuit drives from one port, and detects the signal at the other terminal of the device. Figure 3.4 is the schematic of this alternate circuit. The input and output ports are 50 Ω terminated to eliminate reflections of RF power. Of course, this results in a loss of signal at the output due to the voltage division. It turns out that the 50 Ω resistor on the output side is not necessary because the transmission line is already matched to 50 Ω. The extra resistor reduces our output signal by a factor of two.
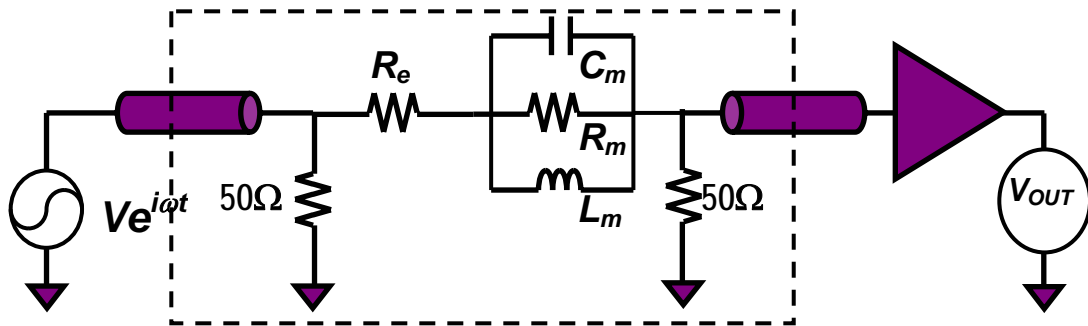

Figure 3.4: Electrical schematic of measurement circuit for high impedance samples.

With this electrical setup, the resonance appears as a dip in the transmitted power to the output port. The impedance of the resonator can be calculated by simple circuit

analysis. For a total resonator impedance $Z_S(f) >> 50\ \Omega$, the output voltage at the input to the preamplifier is

$$\frac{V_{out}}{V_{in}} \approx \frac{25\Omega}{Z_S + 25\Omega} \approx \frac{25\Omega}{Z_S} \quad \text{where } Z_S(f) = R_e + (L_m\ //\ R_m\ //\ C_m) = R_e + Z_m(f).$$

The factor of 25 Ω is due to the 50 Ω termination of the detect line in parallel with the 50 Ω input impedance of the preamplifier. The resonance appears on top of a large background signal which can be removed by dividing it out. We do this by estimating the background amplitude V_b at each point in the resonance using a linear approximation off of resonance. The electromechanical impedance $|Z_m(f)|$ can be easily extracted using the background from,

$$\frac{|Z_m(f)|}{R_e} \cong \frac{V_b - V_{out}}{V_b}.(3)$$

The resonance curve indirectly measures the oscillation amplitude because the back EMF is proportional to the velocity of the beam. The displacement can be easily found by multiplying the left side of (3) by $V_{in}/\zeta Bl\omega_0$. This overestimates the displacement slightly because of unaccounted losses in the signal lines.

3.4   Nanowire resonator results

Due to the fact that the sample resonance is expected to be in the tens of megahertz frequency range, on chip cross talk between the signal lines is a problem. The impedance of the device is about 500 Ω, much greater than the 25 Ω seen at the output port. If the parasitic capacitive coupling impedance ($1/j\omega C$) between the input and output

lines is comparable to 25 Ω, then the RF signal will not pass through the resonator. To deal with this problem, the stray capacitance was minimized with a sample holder that surrounds the sample with ground planes.
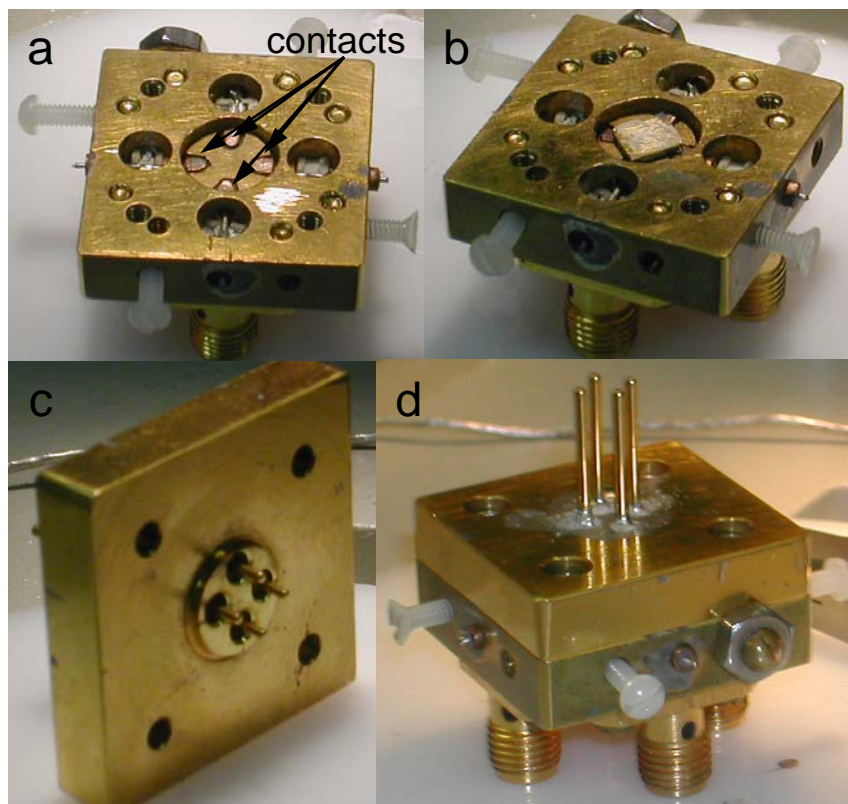

Figure 3.5: (a) Sample holder with four gold contact pads exposed; (b) Sample placed on indium beads to contact pads; (c) Cap with pogo-pins; (d) Assembled sample holder to fully shield sample (Images from Henk Postma).

The sample was mounted into a special sample holder, designed and constructed by postdoc Henk Postma, to prevent cross-talk between the signal leads. Figure 3.5 shows images of the sample holder. The sample is designed with Au leads and pads to contact the sample holder. To mount the chip with the resonator on it, first small beads of indium are placed on the contacts labeled in Figure 3.5a. Next, the chip is inverted

onto the contacts such that the on-chip pads lay on the indium beads (Figure 3.5b). The cap of the sample holder, shown in Figure 3.5c, is carefully placed over the top and fixed with screws (Figure 3.5d). The cap has spring loaded contact pins (pogo-pins) to place force on the chip to ensure good contact between the chip and the sample holder. In addition, the pins on the cap make contact to the back side of the chip. The degenerate Si of the wafer forms a ground plane only 300 nm from the device. The sample is entirely surrounded by a grounded, metallic structure, and the whole sample holder is Au plated for low resistance. Through launchers mounted on the holder, the resonator is electrically connected to RF cables to supply power to the device.

The mounted sample is placed into the vacuum space of a magnet cryostat which can be ramped up to 8 T. Since it is superconducting, the magnet and sample must be cooled with liquid He (4.2 K). The sample is protected by enclosing it in a metal dip stick that is evacuated to 1×10^{-6} torr. The dipper must be evacuated due to the low temperature that the experiment is operated at. Pumping it out prevents gas from condensing on the sample, potentially destroying the device or damping the mechanical resonance. Operating the resonator at low pressure also increases its quality factor due to the lack of damping from air molecules.

After mounting, we measured the resonance characteristics using the technique described above. A network analyzer provides the stimulating RF current to actuate the sample as well as the meter to detect the transmitted signal. By sweeping the frequency of the current, we can locate the resonance and characterize its properties.
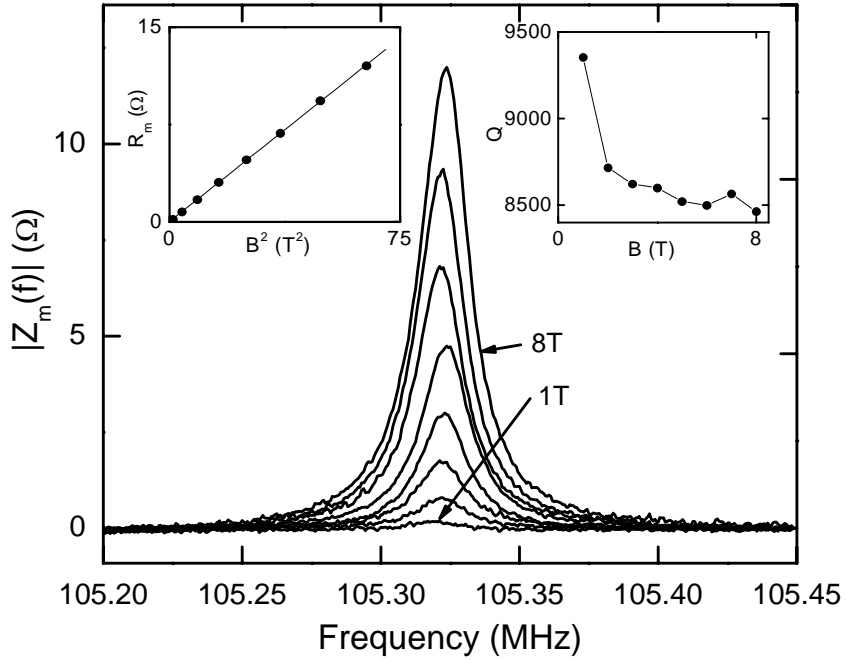
Figure 3.6: Electromechanical impedance vs. frequency for platinum nanowire resonator for increasing magnetic field. Inset Left—B^2 dependence of peak electro-mechanical impedance. Inset Right—quality factor vs. magnetic field.

The resulting curves are plotted in Figure 3.6. Plotted in the left inset, the electromechanical impedance increases with a B^2 dependence, characteristic of magnetomotive drive as predicted by equation (2). The quality factor decreases with increasing magnetic field, as shown in the right inset of Figure 3.6. Some of the decrease can be explained by dissipation of the back EMF through the output resistance it sees. This resonator has a quality factor higher than that of other, "top-down" fabricated beams of comparable size. Carr et al.,[13] for example, measure quality factors for single crystal Si beams and find that Q decreases from about 3000 for beams with a surface area-volume ratio of 0.02 nm^{-1} to a value of 1000 for devices with a ratio of 0.06 nm^{-1}. The nanowire device described here possesses a surface area-volume ratio of 0.095 nm^{-1} and Q of 8500, highlighting an advantages of bottom-up materials—lower surface dissipation. Smaller

materials have a large surface area to volume ratio, and hence greater dissipation from surface states. Top-down fabrication processes can cause damage and defects such as etch roughness that increase surface dissipation.

The frequency of the beam is nearly a factor of two larger than the predicted frequency of 64 MHz. Anecdotal evidence offers some clues as to the reason for this discrepancy. When the dipstick was placed into the liquid helium cooled dewar/magnet, the sample frequency gradually drifts higher until it stabilizes after several hours. This suggests that the frequency is affected by the temperature of the sample. The most likely explanation is that differential thermal contraction in the sample, namely between the metal layer and the Si/SiO$_2$ substrate, introduces tension into the beam, increasing the frequency. By taking the coefficients of linear expansion of Si and Au, the strain ε in the beam is estimated to be about 0.003. The tension T can be can be computed from $T = \pi r^2 \varepsilon Y$ and then taking an approximation of the frequency in the presence of tension,[14]

$$f_T = f_0 \sqrt{1 + \frac{L^2 T}{4\pi^2 YI}}$$

where the moment of intertia $I = \pi R^4/4$. We find a predicted frequency of 94 MHz, in good agreement with the measurement.

When driven with a large enough AC current, the resonator begins to show non-linear characteristics, shown in Figure 3.7. The oscillation amplitude of the resonator shows a hysteresis in the frequency sweep, with the measurement shown in the inset. The details of the nonlinear behavior are fully described in the next section.
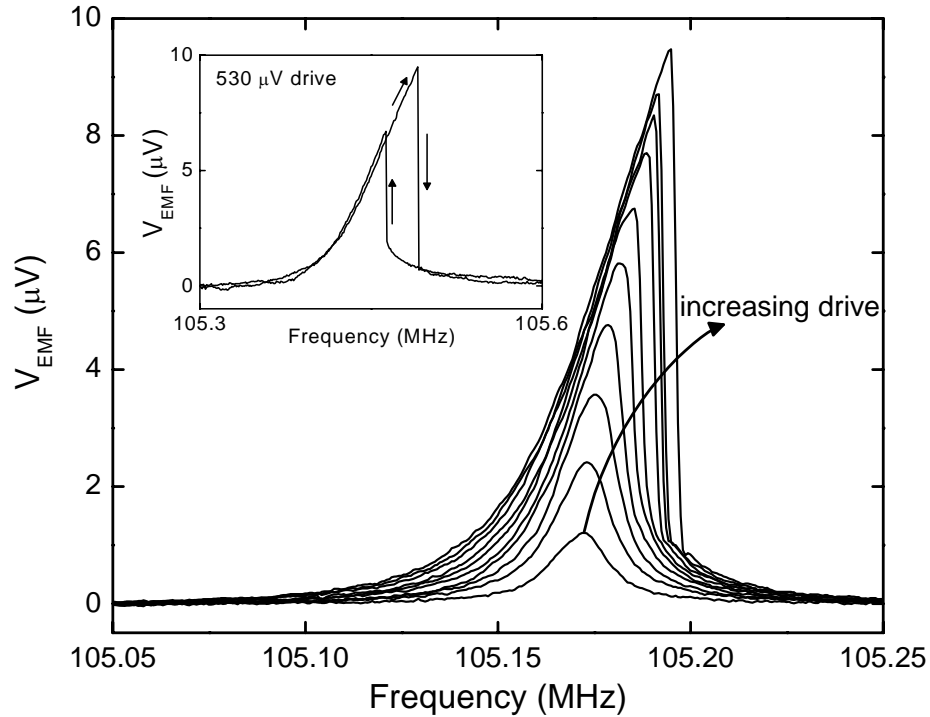
Figure 3.7: Back EMF vs. frequency showing transition to nonlinear resonance with increasing drive. Inset—hysteresis when sweeping frequency up and down.

Note that the resonance frequencies for the plots in Figure 3.7 and inset are different. The resonance would shift slightly if the temperature of the sample was cycled from 4 K to room temperature and back again.

3.5   Non-Linear Mechanical Resonance

In the previous section, we described the initial nonlinear effects measured from the nanowire resonator. This section will describe in detail the theory of the Duffing oscillator. We observed many of the behaviors covered in this section. The remainder of the sections in this chapter will describe further experiments where these effects were measured.
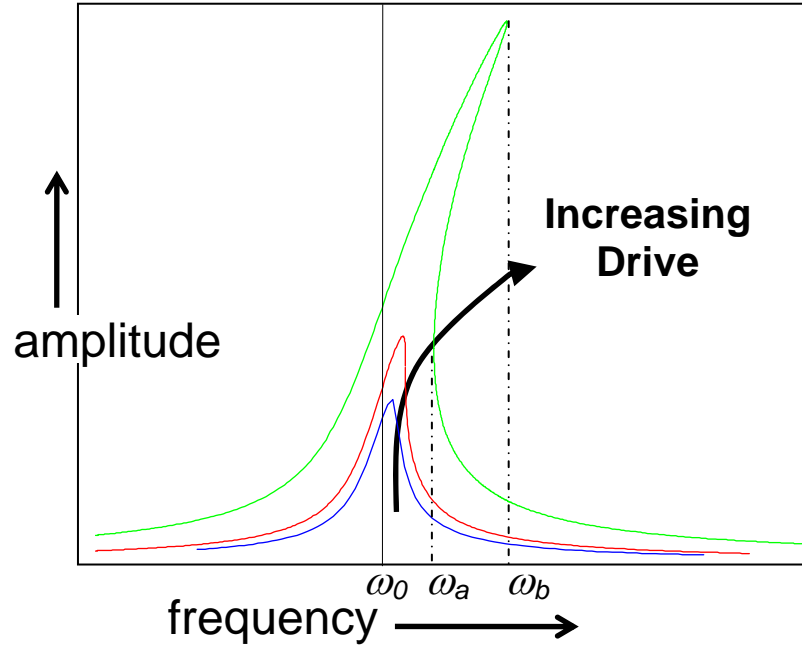
Figure 3.8: Oscillation amplitude vs. frequency for increasing drive strength. ω_o is the frequency in the absence of non-linear behavior.

The non-linear behavior observed arises from the increased tension of the beam as it resonates. At large amplitudes of oscillations the change in the beam length, i.e., the stress on the beam, at the extremes of the motion becomes significant, resulting in a periodically varying tension. Qualitatively, this increases the spring constant of the beam, shifting the resonance frequency, but also distorting the shape of the resonance curve. The increased spring constant increases the frequency, pulling the resonance curve peak to the right at large oscillation amplitudes. Figure 3.8 is a theoretical graph of this distortion for increasing drive amplitude showing the distortion in the resonance curve shape.

We can introduce nonlinearity into resonator theory in a number of ways. It is interesting to contrast the methods of Landau & Lifshitz (L&L)[15] vs. Nayef & Mook

(N&M).[16] Through two seemingly dissimilar methods, both derivations reach an identical equation to describe the Duffing oscillator. For full derivation, see references. I will briefly outline the method and result of each below.

L&L begin by considering the Lagrangian of an anharmonic oscillator expanded up to the fourth order nonlinear term,

$$L[x(t)]: \frac{1}{2}m\dot{x}^2 - \frac{1}{2}m\omega^2 x^2 - \frac{1}{3}m\alpha x^3 - \frac{1}{4}m\beta x^4,$$

and from it, derive the equation of motion which has a third-order restoring force. By successive approximate solutions to the equation of motion, they find a correction to the frequency that is second-order in the amplitude of oscillation. Finally, L&L substitute the correction into the solution of the linear equation of motion for a driven, damped harmonic oscillator to derive an equation that is sixth-order in the amplitude, a:

$$\kappa^2 a^6 - 2\varepsilon\kappa a^4 + (\varepsilon^2 + \lambda^2)a^2 = \frac{D^2}{4\omega_0^2} \quad (3)$$

where ε is the detuning from the linear frequency ω_0, D is the drive, κ is the non-linear coefficient, and λ is the damping constant.

In contrast, N&M begin with the Duffing equation, which is a directly driven system with cubic nonlinearity,

$$\ddot{x} + \omega_0^2 x + 2\varepsilon\mu\dot{x} + \varepsilon\alpha x^3 = \varepsilon k \cos[(\omega_0 + \varepsilon\sigma)t].$$

A method of multiple timescales is used to find an approximate solution. Taking the steady state in amplitude, frequency and phase, N&M derive a frequency response equation which is once again sixth-order in the amplitude, a:

$$\left[\mu^2 + \left(\sigma - \frac{3\alpha}{8\omega_0}a^2\right)^2\right]a^2 = \frac{k^2}{4\omega_0^2} \quad (4)$$

where σ is the detuning frequency from ω_0, k is the drive, α is the non-linear coefficient, and μ is the damping constant. Equations (3) and (4) are perfectly identical if one equates $\kappa = 3\alpha/8\omega_0$. It is somewhat remarkable and very comforting that these two authorities agree. By apparently different approximations L&L and N&M arrive at the same behavior for the Duffing oscillator. L&L's approach is much more intuitive and is derived from fundamental physics. N&M's method is basically an approximate solution to a non-linear differential equation. It is more analytical and also can be used to predict the non-resonant transients of a moving beam. Our measurements will show that the Duffing oscillator well describes the non-linear oscillation properties of our beam.

From the frequency response equation (4), one can describe the amplitude vs. frequency plot, often referred to as a "Tsunami" curve which is graphed in Figure 3.8. At high enough drive strengths, the curve pulls to the right (for $\alpha > 0$), creating a tri-valued region which, for the green curve, is between the frequencies ω_a and ω_b. A stability analysis shows that the middle branch of the three is unstable, so that in measurement a hysteresis is observed. When sweeping the frequency from low to high, the amplitude follows the upper branch until the frequency reaches ω_b, and then switches suddenly to the lower amplitude state. Similarly, the switch is from low to high amplitude is at ω_a when sweeping down in frequency.
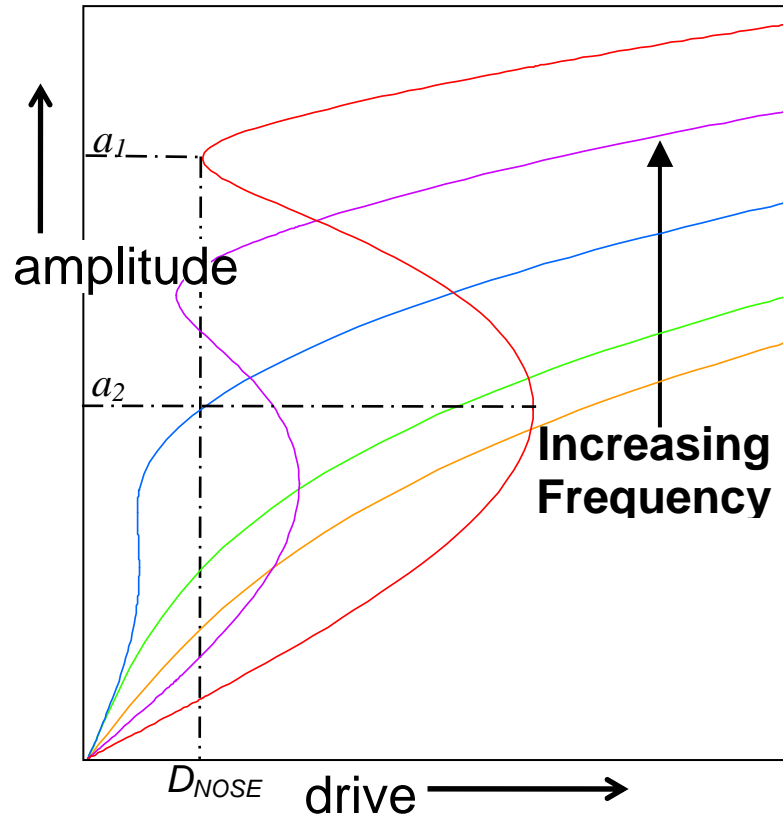
Figure 3.9: Amplitude vs. drive strength for increasing frequency from linear resonance frequency ω_0.

This hysteresis is visible in phase vs. frequency, output amplitude vs. drive amplitude, and phase vs. drive amplitude sweeps. The exact frequency or drive amplitude at which the resonator switches states is subject to some variation due to noise. Section 3.7 investigates this effect further. For a frequency sufficiently detuned from ω_0, as the drive is increased, the oscillation amplitude will switch to the upper branch discontinuously. Figure 3.9 shows the amplitude vs. drive for increasing frequency from the linear resonance frequency ω_0.

For the purpose of observing non-linear behavior such as the basins of attraction described in the next section, a second resonator was fabricated with length of about 2.2

µm, pictured in Figure 3.10. This beam has a predicted frequency of 26 MHz, but a measured frequency of about 45 MHz, probably because of differential thermal contraction of the sample, as observed similarly in the first resonator.
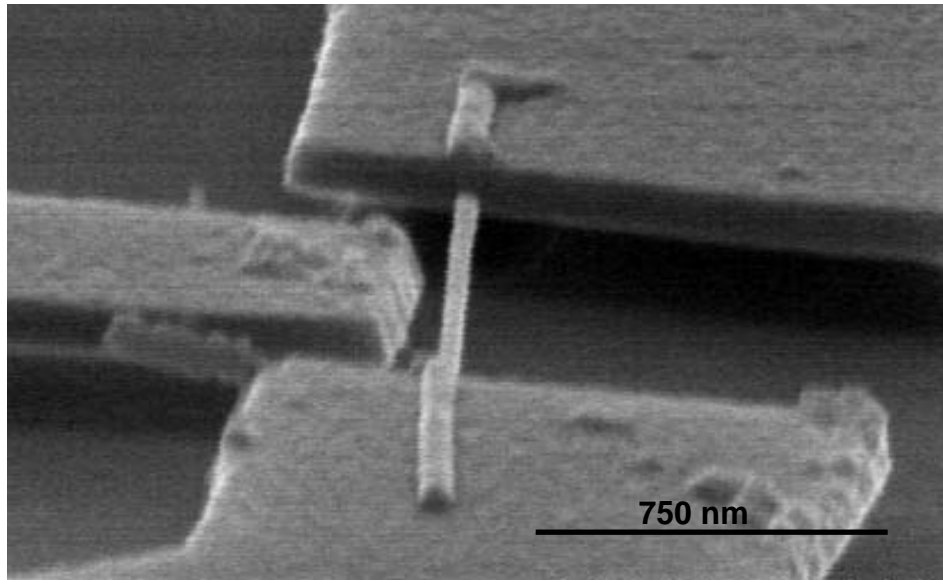

Figure 3.10: SEM image of resonator measured for non-linear studies.

The resonance behavior of this sample is shown in Figure 3.11. For increasing drive amplitude, the resonance curve becomes distorted and hysteretic behavior is observed, as expected. The right graph shows experimental verification of the hysteresis in phase. In each graph, the final two curves are at the same drive amplitude but with the frequency swept in the opposite direction, as indicated by the arrows. Experimentally, the sample can be arbitrarily prepared in the upper or lower stable states simply by sweeping the frequency or drive amplitude from the appropriate direction.
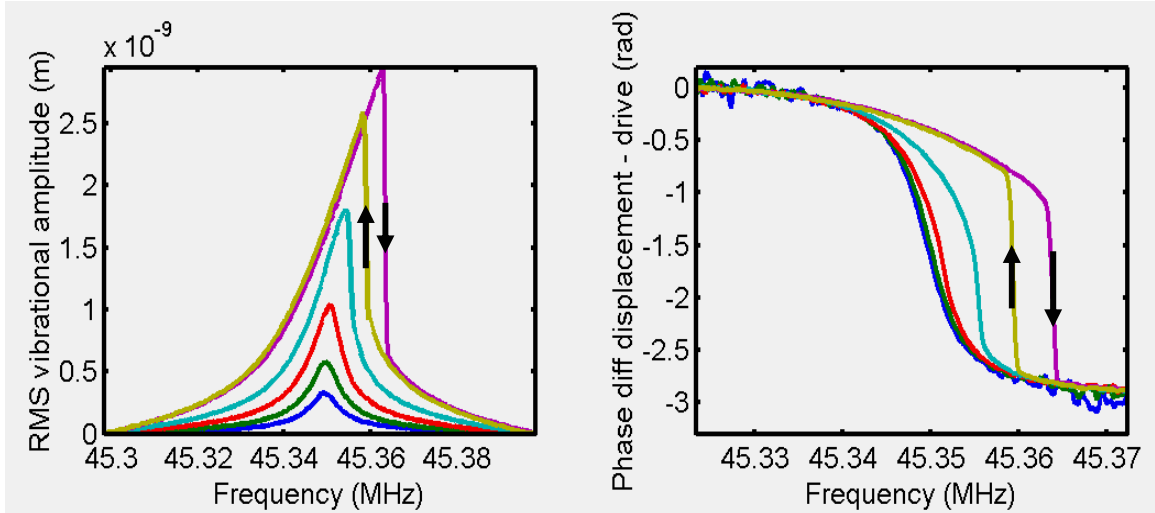
Figure 3.11: Left—vibration amplitude vs. frequency for increasing drive amplitude. Right—phase vs. frequency for increasing drive amplitude. The final two curves in each plot are at the same drive strength, but opposite sweep directions, indicated by the arrows.

3.6   Mapping of the state plane

At a drive larger than the critical drive and a frequency within the tri-valued region (between the frequencies ω_a and ω_b in Figure 3.8), one can plot the phase, with respect to the drive, and the amplitude of the resonator in a polar fashion. Figure 3.12, generated by our theoretical collaborator Oleg Kogan, shows such a plot, called a state plane, with an inset showing the resonance shape and frequency of interest. The three points marked (known as fixed points) correspond to the three points where the resonance curve intersects vertical line in the inset. The red curves indicate the path through phase space that the displacement would take if going from the unstable state B to one of the stable states, A or C. The "ying-yang" shape divides the plane into "two basins of attraction" corresponding to the two stable states. The boundary between the basins is

referred to as the separatrix. A resonator with initial condition of phase and amplitude within one of the basins will settle to the stable state within that basin.[16]
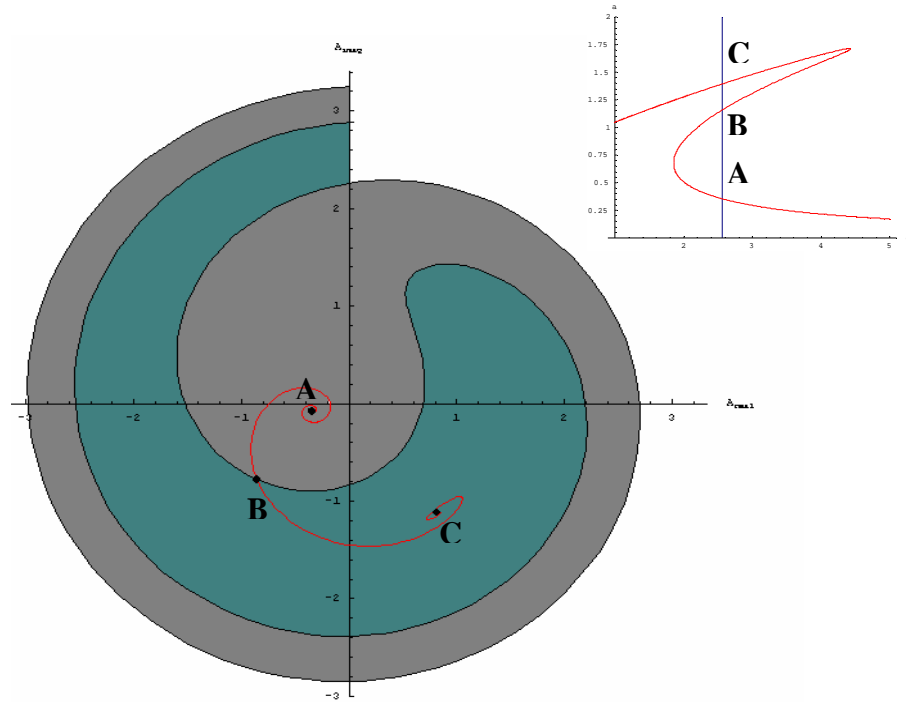

Figure 3.12: Theoretical plot of state plane of the Duffing oscillator. The axes are in-phase and out-of-phase displacement of the beam. Inset—Frequency corresponding to state plane, with respect to resonance curve.

One of our primary goals from research on non-linear resonator was to experimentally measure the separatrix and basins of attraction associated with the Duffing oscillator. The procedure for such a measurement begins with selecting an oscillation frequency for which the device has two stable resonance amplitudes for a large enough driving amplitude. The resonator is driven with some power at this frequency, and the amplitude and phase of the resonance is measured. Next, the drive signal is changed quickly to a final drive amplitude strong enough to produce bistability. The state of the resonator is measured to determine which of the two stable amplitudes

resulted. The relative phase of the two drive signals is varied, tracing a circle in the resonator phase plot. The schematic for this experiment is shown in Figure 3.13. Of particular importance in this setup is the switch that changes from the initial drive to the final drive. Attempts to achieve this measurement with a slower switch (Mini-circuits ZMSW-1211, switching time: 2 μs) were unsuccessful. It is important that the switch be faster than the oscillation frequency of the resonator. The one used (Mini-circuits ZASWA-2-50DR) has a specified switching time of 10 ns.
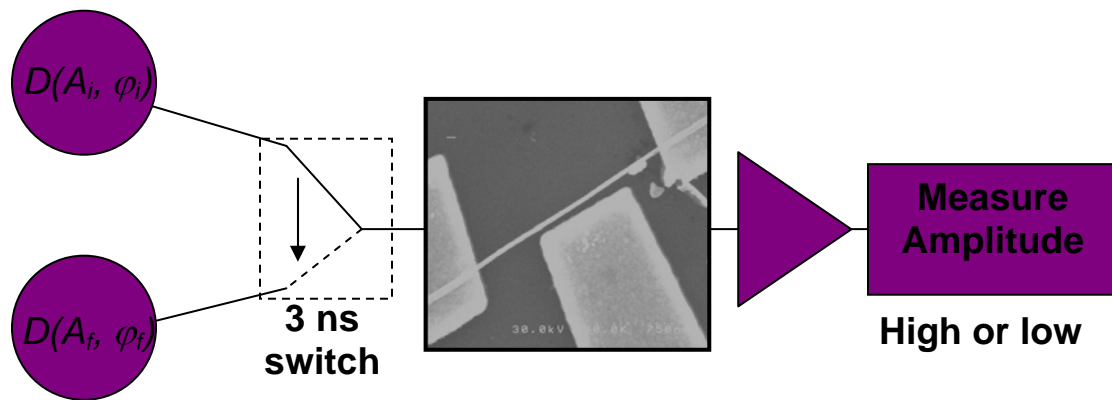
Figure 3.13: Schematic of measurement of basins of attraction of Duffing oscillator. The amplitude and phase of the resonator's drive signal is suddenly switched.

Figure 3.14 plots the data from this initial experiment. This data traces a circle in the phase space of the oscillator, centered at the origin. This is consistent, since the amplitude of the initial drive, and hence the beam displacement, was kept constant while the phase, with respect to the final drive signal, is rotated through 360 degrees. In this plot, one can see a clear transition between relaxing to the upper state and relaxing to the lower state after switching the drive signal.
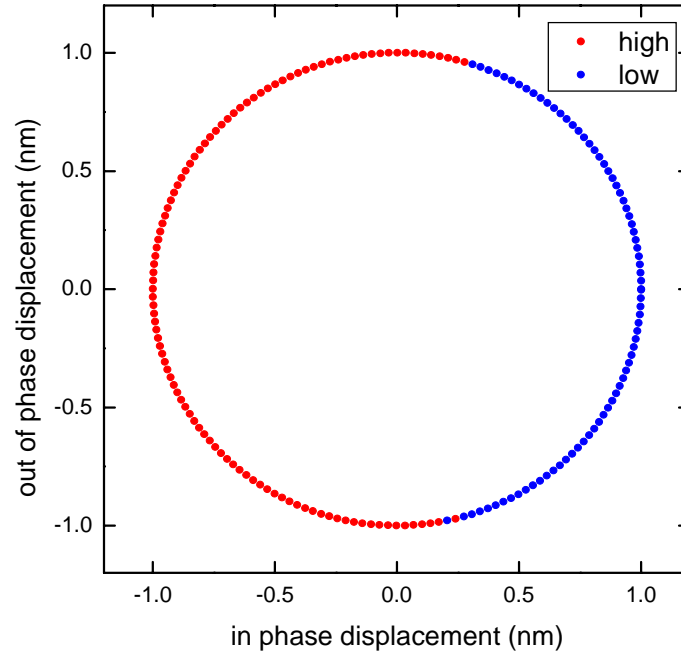
Figure 3.14: Resonator phase plot of final state with respect to initial phase for a fixed initial drive amplitude. To fully map the state plane the initial drive amplitude will be varied.

To map out the whole state plane, the data for Figure 3.14 was collected for a range of driving amplitudes. Figure 3.15 plots our first attempt to measure the basins of attraction of the resonator. There is a glaring gap in the initial amplitudes that we can access. This can be easily explained by referring to Figure 3.9. For the frequencies that exhibit hysteresis there is a range of amplitudes where there are no stable oscillation states. For example, for the detuning frequency corresponding to the red curve, there are not stable resonance amplitudes between a_1 and a_2 for any driving strength. Therefore, at this frequency we cannot access those amplitudes with the current electronic setup. This problem will be addressed later.
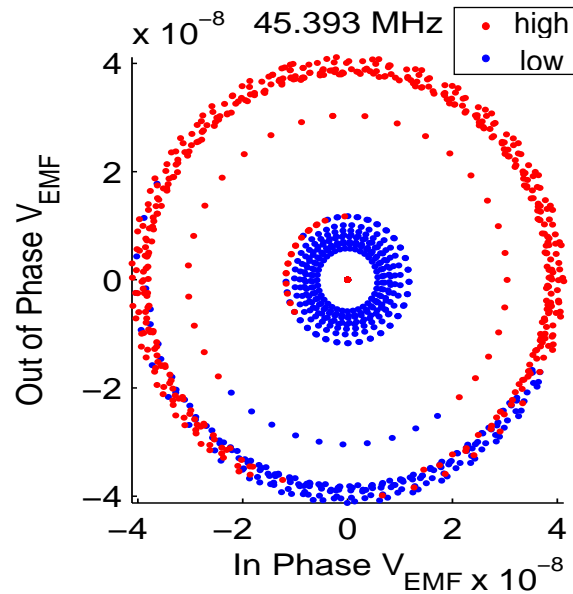
Figure 3.15: Experimental measurement of basins of attraction. Red and blue correspond to the high and low amplitude stable states, respectively.

We repeated the experiment of Figure 3.15 for multiple frequencies within the hysteretic region. As the frequency is changed, corresponding to moving across the hysteresis, the two basins of attraction should exchange area, as depicted in Figure 3.16. Toward the left side of the tri-valued region, the high amplitude state dominates the state plane. As the frequency is swept to the right the low amplitude basin increases in area at the expense of the other. Figure 3.17 shows experimental results of changing frequency. Indeed, the basin corresponding to the low amplitude final state (blue) increases in area at the expense of the high amplitude state (red).
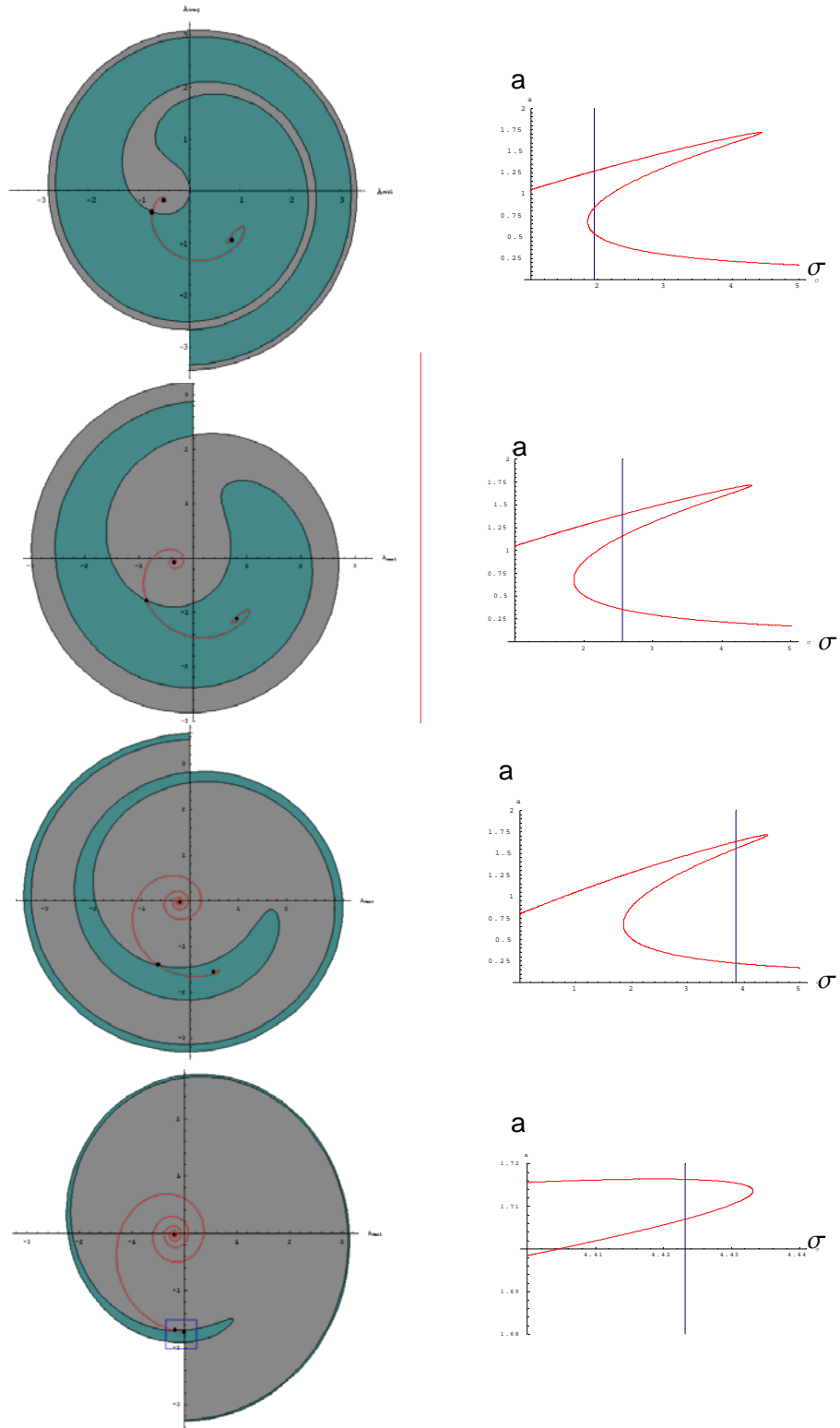
Figure 3.16: Exchange of area of basins of attraction as frequency is varied across tri-valued region (Images from Oleg Kogan).

We also expect an exchange of area when keeping the frequency constant and varying the final state driving strength. The results of the experiment are plotted in Figure 3.18. When increasing the driving strength, the Tsunami curve of Figure 3.8 stretches to the right so that both ω_a and ω_b increase. If the measurement is performed at fixed frequency, then decreasing the drive strength is similar to increasing the frequency in terms of the area exchange of the basins of attraction. The measurement bears this out.
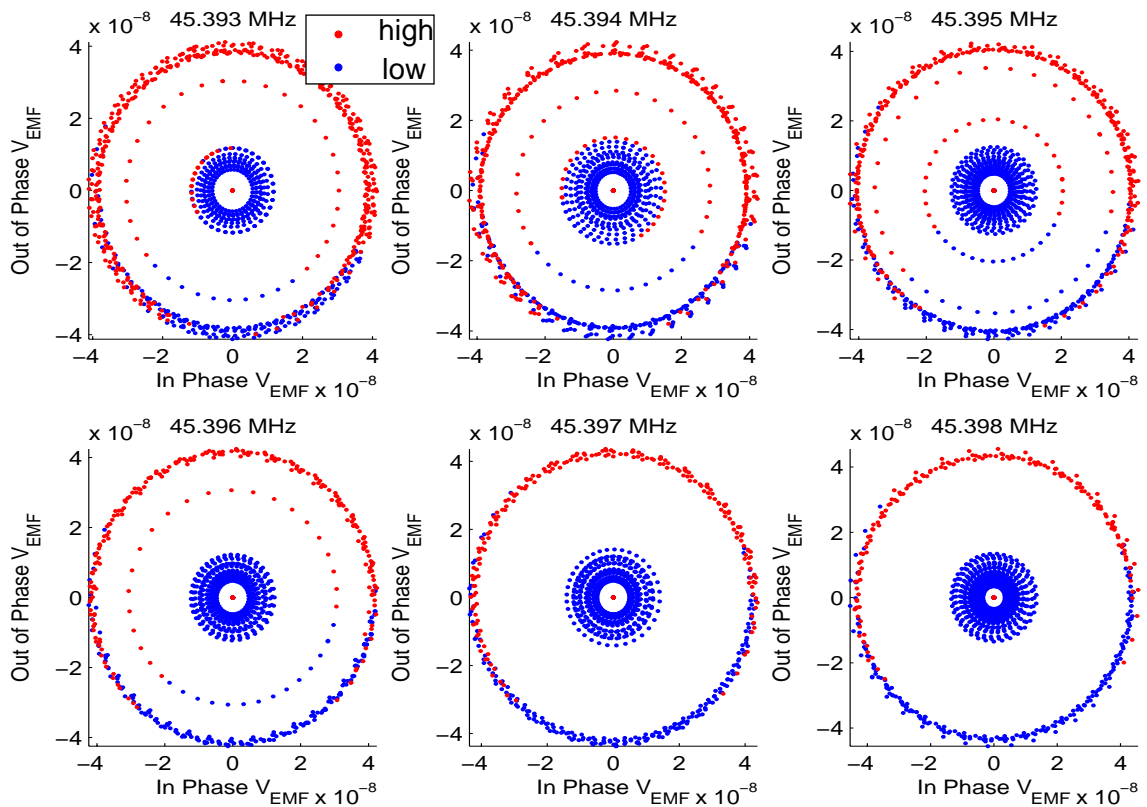

Figure 3.17: Experimental measurement of basins of attraction as frequency is varied through tri-valued region. As the frequency is increased, the low amplitude (blue) basin grows.
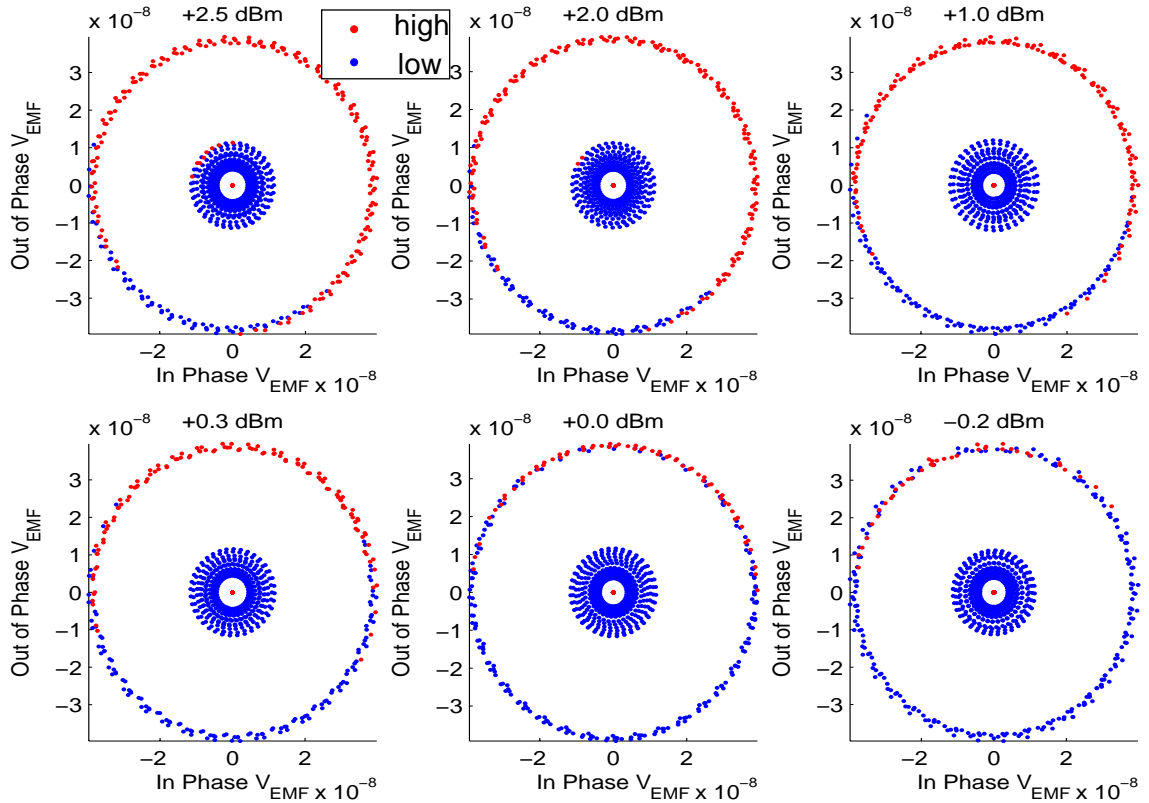
Figure 3.18: Experimental measurement of basins of attraction of resonator for decreasing drive strength. Drive strength is before attenuation. Drive strength at sample is about -70 dBm.

All the data plots of Figures 3.17 and 3.18 have inaccessible regions where there are no stable resonance amplitudes for any drive. However, we can access these regions by use of the gate to shift the frequency. Figure 3.19 plots the variation in the frequency for a DC bias applied either to the gate or directly to the nanowire, where in the latter case, the substrate acts as the gate. Applying bias the directly to the nanowire clearly has a much larger effect, most likely because the resonator has a larger capacitance to the substrate than to the side gate. The frequency decreases with applied voltage, though the result we would expect is not clear. The electrostatic force on the wire should increase its tension, increasing the frequency. However, the electrostatic force itself, when the

variable capacitance is taken into account, lowers the spring constant, decreasing the frequency. We do not understand the slight rise in frequency as very small bias voltages seen in both gate biased and wire biased data. The data indicates that the latter is the dominant effect.
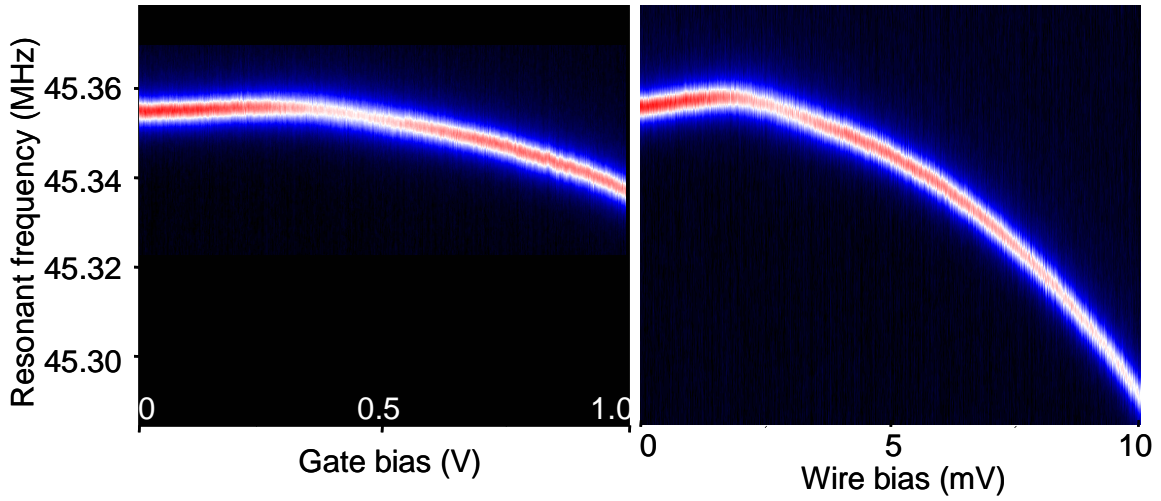

Figure 3.19: Frequency of resonance peak as a function of DC gate voltage. Left—bias on side gate. Right—bias on wire. The color shows the amplitude of the oscillation.

The intermediate amplitudes can now be accessed by tuning the resonant frequency of the beam. Because the gate lowers the frequency of the beam, the DC bias must be applied to the final drive amplitude side as diagramed in the modified measurement apparatus in Figure 3.20. One can understand why the bias is applied to the final drive amplitude side by reference to Figure 3.9. With the bias, the frequency of the state plane corresponds to the red curve with inaccessible amplitudes. However, without the bias, the same frequency corresponds to the green curve, allowing us to access those amplitudes for the initial state. Following the procedures used to collect the data of Figures 3.17 and 3.18 above, with a DC bias of 11 mV, the drive switching experiment

was repeated again for a range of driving strengths, again varying the relative phase of the initial and final drive signals.
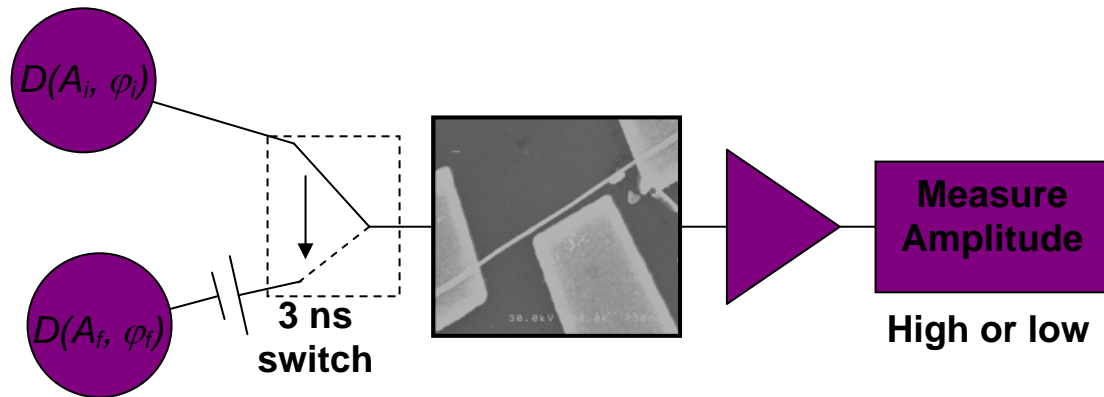

Figure 3.20: Modified measurement setup for measurement of state plane with DC bias of 11 mV added to final drive signal.

Figure 3.21 has plots of the results. To show the basins of attraction clearly, the plot has been recolored in the following way: the state plane was divided up into pixels and the color of each pixel determined by the color of the nearest data point. We have successfully measured the ying-yang shape of the basins of attraction. As the drive strength is increased, the upper state becomes dominant, covering the whole plane. The boundary between the two basins is not well defined due to a number of effects. Noise obviously plays a part in blurring the boundary; its role in switching between stable oscillation modes is addressed in the next section. Additionally, there is no control over any electronic transients that may appear as a result of switching the drive signal. Transient current in the resonator will result in non-resonant forces on the beam that can kick it over the separatrix in a similar manner as noise. It should also be noted that the system we originally set out to study has been modified through the use of gating.
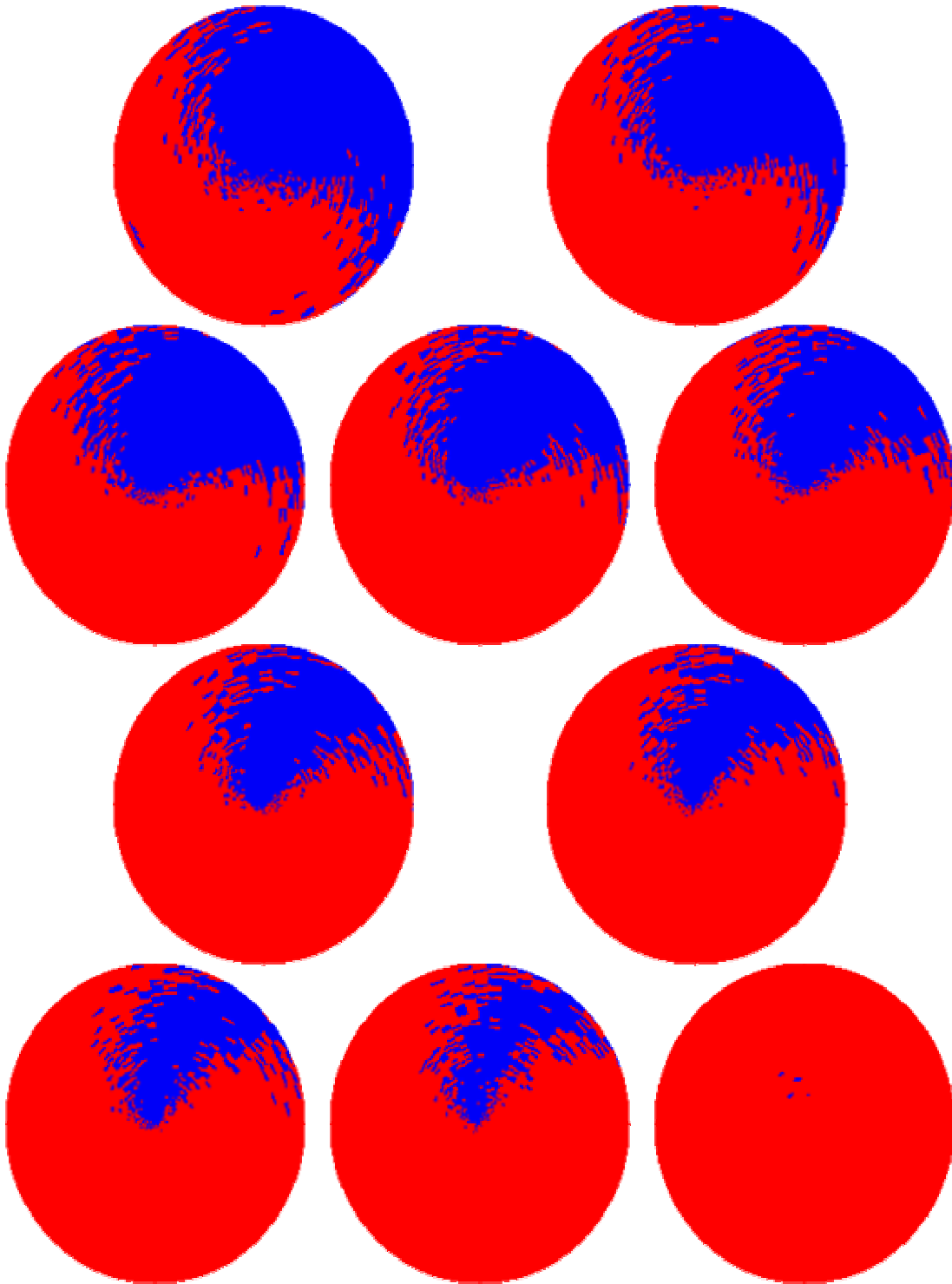
Figure 3.21: Experimental map of platinum nanowire resonator state plane for increasing drive strength from left to right, top to bottom.

3.7   Noise Induced Switching

The effects of noise on physical systems are important to investigate in any experiment. In the non-linear resonator, noise will cause the resonator to switch branches before the tri-valued region has been fully traversed. Figure 3.16, lower left graph, helps to explain this effect in terms of the stability basins. When the resonator is in the upper stable state, within the small area basin, noise can easily "kick" it over the separatrix. Once this boundary is crossed, the sample will settle to the lower stable state. However, the reverse process requires a much larger noise power because the basin boundary is far away from the lower stable state.

We investigated the impact of noise on spontaneous switching at frequencies close to the edge of the hysteretic region in a variety of ways. Initially, the resonator was prepared in the lower state close to the left edge of the tri-valued region. The amplitude of the oscillation is observed until it switches to the upper state and the time is recorded. This process is repeated many times. The wait times are tabulated as a histogram in Figure 3.22.
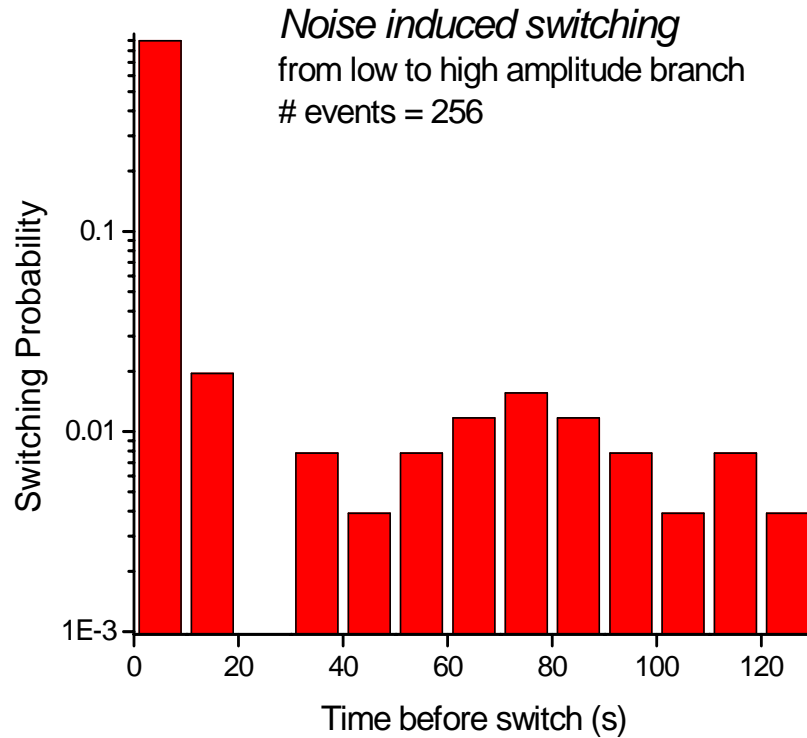
Figure 3.22: Probability of switching event within 10 second intervals. Total number of events is 256.

The wait times are long in the previous experiment, restricting the amount of data we can take. In order to collect a statistically useful amount of data, the experiment was modified by adding a broad-band (white) noise source to the drive line to increase the switching rate. The resonator is again prepared in the lower state at a frequency farther from the left side of the hysteresis, the resonance is monitored until it switches to the upper state, and the time recorded. The procedure is repeated to get enough switching events to perform meaningful statistics. With this data we can plot the probability that the resonator has switched *P(t)* versus time for various noise powers, shown in Figure 3.23. As the noise power is increased, the switching probability for a particular time increases, as one would expect.
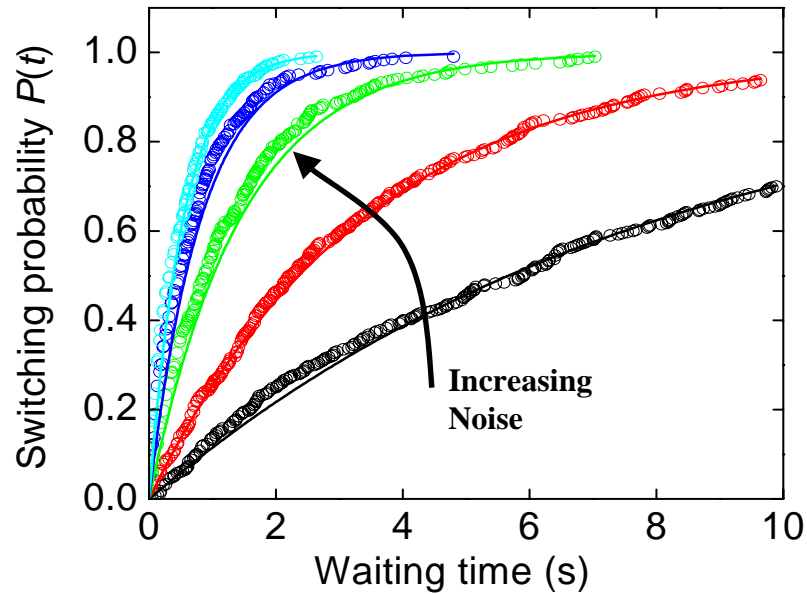
Figure 3.23: Switching probability vs. waiting time for increasing noise power. The solid line is theoretical fit of equation 4. Each curve is 5000 switching events.

The theoretical model, derived by our theorist collaborators Oleg Kogan and Mike Cross, predicts that the probability of switching should follow

$$P(t) = 1 - e^{-t\Gamma}, \quad (4)$$

where $\Gamma \propto \delta^{1/2} \exp\left(\dfrac{-A\delta^{3/2}}{\langle x^2 \rangle}\right),$

$\langle x^2 \rangle$ is the noise power, A is a factor on the order of unity that depends on the frequency detuning from ω_0, and $\delta = D - D_{NOSE}$. D_{NOSE}, marked in Figure 3.8, is the value of the drive at the left side of the hysteresis in drive amplitude. If the process of switching is considered akin to noise kicking the resonator over an energy barrier, the theory implies a barrier height of $A\delta^{3/2}$. We will seek to verify this prediction.
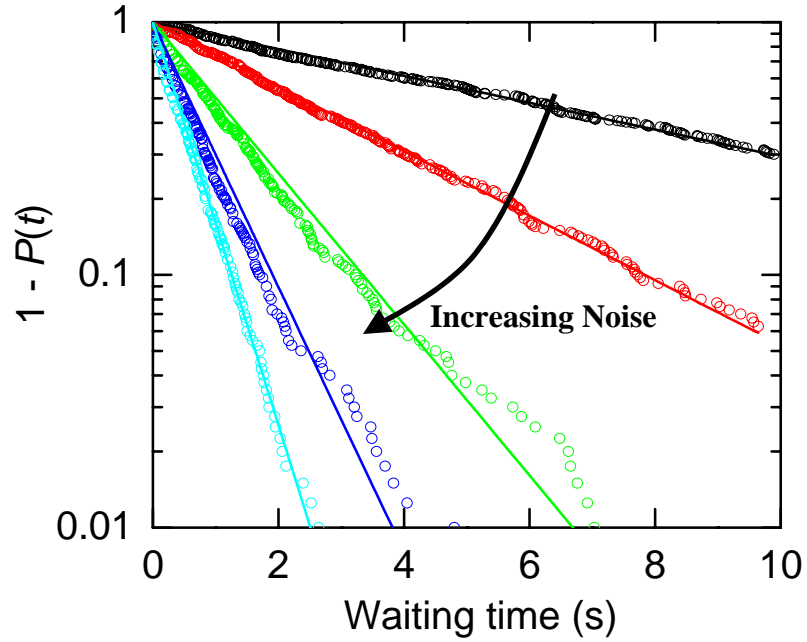
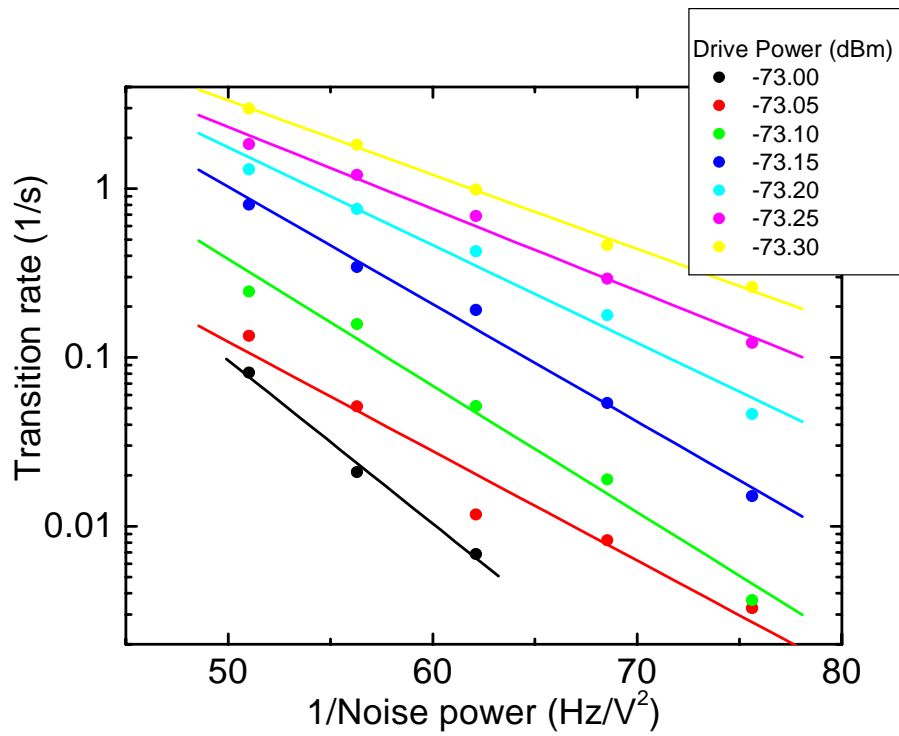Figure 3.24: Semilog plot of 1-*P(t)* vs. waiting time for increasing noise power.

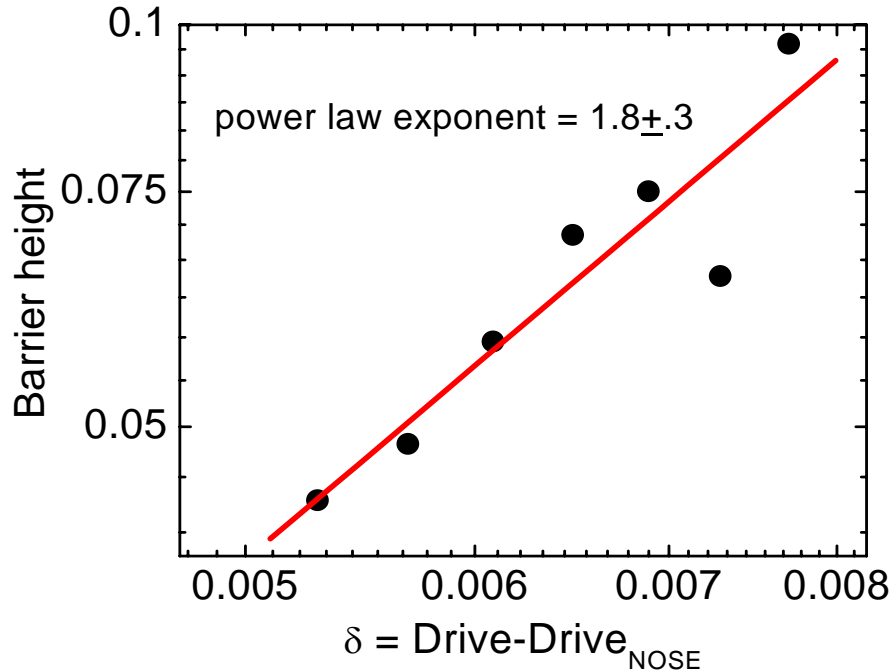Figure 3.25: Transition rate vs. 1/(noise power) for varying drive power.

Figure 3.26: Effective energy barrier height vs. driving power. The slope of the line matches with the theory.

By plotting $1\text{-}P(t)$ on a semilog axis, as in Figure 3.24, the transition rate Γ for each noise power can be extracted from the slope of the line. The data of Figure 3.24 was collected for a range of drive strengths D, extracting Γ for each. For each D, the transition rate was plotted against 1/(noise power) again in a semilog plot, shown in Figure 3.25. From the slope of each line in Figure 3.25, the barrier height $A\delta^{3/2}$ can be calculated. Finally, in Figure 3.26, the barrier height is plotted against δ in a semilog plot for the third time. We find that the exponent for δ in the barrier height is 1.8 ± 0.3, in approximate agreement with theory.

3.8   Summary

In this work we have fabricated the first doubly-clamped resonators constructed from "bottom-up" materials, platinum nanowires with diameters about 40 nm and lengths of 1-2 µm.   We have developed techniques to detect the resonance modes of high impedance (> 50 Ω), radio frequency devices with magnetomotive techniques and have measured the resonance characteristics of such devices.   Our devices exhibit a quality factor much larger than "top-down" fabricated resonators of a comparable size, probably because of reduced surface dissipation.

Non-linear effects arise at relatively low driving amplitude.   We have measured the basins of attraction of the beam, verifying that the Duffing oscillator is a good model for the non-linear effects observed.   Switching between stable resonance amplitudes is observed and the influence of noise on switching was tested.   The results follow the theoretical model for the switching rates well.

References

[1]   M. D. LaHaye, O. Buu, B. Camarota et al., "Approaching the quantum limit of a nanomechanical resonator," *Science* **304** (5667), 74-77 (2004).

[2]   A. N. Cleland and M. L. Roukes, "Fabrication of high-frequency nanometer-scale mechanical resonators from bulk Si crystals," *Applied Physics Letters* **69** (18), 2653-2655 (1996).

[3]   Y. T. Yang, K. L. Ekinci, X. M. H. Huang et al., "Monocrystalline silicon carbide nanoelectromechanical systems," *Applied Physics Letters* **78** (2), 162-164 (2001).

[4]   D. A. Harrington, P. Mohanty, and M. L. Roukes, "Energy dissipation in suspended micromechanical resonators at low temperatures," *Physica B* **284**, 2145-2146 (2000).

[5]   A. N. Cleland, M. Pophristic, and I. Ferguson, "Single-crystal aluminum nitride nanomechanical resonators," *Applied Physics Letters* **79** (13), 2070-2072 (2001).

[6]   S. Sapmaz, Y. M. Blanter, L. Gurevich et al., "Carbon nanotubes as nanoelectromechanical systems," *Physical Review. B, Condensed Matter and Materials Physics* **67** (23), art.no.-235414 (2003).

[7]   Y. Huang, X. F. Duan, Y. Cui et al., "Logic gates and computation from assembled nanowire building blocks," *Science* **294** (5545), 1313-1317 (2001).

[8]   C. R. Martin, "Nanomaterials - a membrane-based synthetic approach," *Science* **266** (5193), 1961-1966 (1994).

[9]   S. Timoshenko, D. H. Young, and W. Weaver, *Vibration problems in engineering*, 4th ed. (Wiley, New York,, 1974), pp.xiii, 521.

[10]   *CRC handbook of chemistry and physics*. (CRC Press, Cleveland, Ohio, 1977), p.v.

[11]   H. Krommer, A. Erbe, A. Tilke et al., "Nanomechanical resonators operating as charge detectors in the nonlinear regime," *Europhysics Letters* **50** (1), 101-106 (2000).

[12]   A. N. Cleland and M. L. Roukes, "External control of dissipation in a nanometer-scale radiofrequency mechanical resonator," *Sensors and Actuators. A, Physical* **72** (3), 256-261 (1999).

[13]   D. W. Carr, S. Evoy, L. Sekaric et al., "Measurement of mechanical resonance and losses in nanometer scale silicon wires," *Applied Physics Letters* **75** (7), 920-922 (1999).

[14]   H. W. Ch. Postma, I. Kozinsky, A. Husain et al., "Dynamic range of nanotube and nanowire NEMS resonators," Unpublished (2004).

[15]   L. D. Landau and E. M. Lifshits, *Mechanics*, 3rd rev. English , repr. with corrections. ed. (Pergamon Press, Oxford ; New York, 1989), p.170.

[16]   A. H. Nayfeh and D. T. Mook, *Nonlinear oscillations*. (Wiley, New York, 1979), p.704.